Regular Article – Experimental Physics

Measurement of ^{96}Zr(n, γ)^{97}Zr reaction cross section at the neutron energies of 0.61 and 1.05 MeV and covariance analysis for the uncertainty

S. Badwar[1], R. Ghosh[1], B.M. Lawriniang[1], Y.S. Sheela[2], H. Naik[3,a], B.M. Jyrwa[1], Y.P. Naik[4], S.V. Suryanarayana[5], and S. Ganesan[6,b]

[1] Physics Department, North Eastern Hill University, Shillong-793022, Meghalaya, India
[2] Department of Statistics, M.A.H.E, Manipal, Karnataka-576104, India
[3] Radiochemistry Division, Bhabha Atomic Research Centre, Trombay, Mumbai-400085, India
[4] Product Development Division, Bhabha Atomic Research Centre, Mumbai-400085, India
[5] Nuclear Physics Division, Bhabha Atomic Research Centre, Trombay, Mumbai-400085, India
[6] HBNI, Bhabha Atomic Research Centre, Mumbai-400085, India

Abstract. The ^{96}Zr(n, γ)^{97}Zr reaction cross sections relative to ^{197}Au(n, γ)^{198}Au monitor reaction with the neutron energies of 0.61 and 1.05 MeV from the ^{7}Li(p, n)^{7}Be reaction have been measured for the first time by using the activation and off-line γ-ray spectrometric technique. The error analysis of the experimental data was done by considering the partial uncertainties in various attributes and the correlations between those attributes were reported through covariance analysis. The present experimental cross sections have been compared with the theoretical prediction by TALYS-1.8 using the back-shifted Fermi gas model and Brink-Axel Lorentzian γ-ray strength functions. The TALYS-1.8 calculations well predicted the present experimental cross sections at both neutron energies. The spectrum averaged neutron capture cross sections of ^{96}Zr obtained in the present work have also been compared with the evaluated cross sections from ENDF/B-VIII.0, JENDL-4, JEFF-3.3, CENDL-3.1 and TENDL-2015 libraries. They are found to be in close agreement with the TENDL-2015 and CENDL-3.1 libraries at the neutron energies of 0.61 and 1.05 MeV.

1 Introduction

Measurements of neutron activation cross sections and the improved nuclear database of reaction cross sections play a vital role in the design and safe operation of various nuclear systems such as Generation IV nuclear reactors, fusion reactors, and accelerator-driven subcritical systems (ADSs) [1–3]. Neutron-induced activation cross sections have direct applications in estimating the radiation levels and the decay heat of materials that have been exposed to radiation fields with a strong neutron component [4]. In particular, the neutron induced reaction cross sections of structural materials such as Zr, Nb, Fe, Co, Ni and Cr are important from the point of view of neutron economy of the reactor and thus are important for advanced reactor designs. Among these metals, zirconium is highly resistant to corrosion by alkalis, acids, salt water and the other chemical agents. The high resistance to corrosion in aggressive environments at high temperatures makes Zr metal to be appropriate in many applications, such as heat exchangers, pumps, reactor vessels, valves, surgical appliances and chemical industry, where corrosive agents are employed [5]. The Zr metal itself has a low neutron absorption cross section [6–9] for low energy neutrons. Therefore nuclear power industry has the major application of the Zr and its alloy as the structural and cladding materials in ADSs and most of the conventional water reactors. About 90% of the zirconium produced is frequently used in the form of zircaloy for the cladding of fuel rods in nuclear reactors. Zr based alloys containing Sn, Fe and Cr with or without Ni are called Zircaloy-2 and Zircaloy-4. Zircaloy-2 contains 1.5% tin, 0.1% iron, 0.1% chromium, 0.05% nickel, and not more than 0.01% nitrogen. Zircaloy-4 differs from Zircaloy-2 by lower nickel content (0.007%) Zircaloy-2 is used in boiling water reactors (BWR) and

zircaloy-4 in pressurized water reactor (PWR). In pressurized heavy water reactor (PHWR), Zr-2.5wt% Nb alloy is used for pressure tubes [10–12]. In the design of ADSs, ZrN is planned to be utilized as a main constituent of the nuclear fuel pallet.

In all the conventional reactors, the neutrons have very low energy, below thermal to 15–20 MeV. On the other hand, ADSs have a high energy neutron spectrum depending on the proton energy. Thus it is very much necessary to measure the fast neutron induced reaction cross section of different isotopes of zirconium. The spectrum average cross section of ^{96}Zr(n, γ)^{97}Zr reaction in the thermal energy region and at the neutron energy of 30 keV has been measured by various authors [13–16] and are available in EXFOR library [17,18]. The thermal neutron activation cross sections of most of the zirconium isotopes were measured using the reactor neutrons. For the measurement of the ^{96}Zr(n, γ)^{97}Zr reaction cross section at the neutron energy of 30 keV [16], the neutron spectrum from the thick-target ^{7}Li(p, n) reaction setup was simulated by using SimLiT. The EXFOR database indicates that in the earlier measurements of spectrum averaged ^{96}Zr(n, γ)^{97}Zr reaction cross section there are no data available at the neutron energies above 30 keV. Thus in the present work, we measured the ^{96}Zr(n, γ)^{97}Zr reaction cross sections at the effective neutron energies of 0.61 MeV and 1.05 MeV by using activation and off-line gamma-ray spectrometric technique. The neutrons were generated by using the ^{7}Li(p, n) reaction. The measurement of ^{96}Zr(n, γ)^{97}Zr reaction cross sections were done relative to the ^{197}Au(n, γ)^{198}Au monitor reaction. The error analysis of the experimental data was done by considering the partial uncertainties in various attributes. The correlations between those attributes were reported through covariance analysis. The ^{96}Zr(n, γ)^{97}Zr reaction cross section as a function of neutron energy was also calculated theoretically by using the computer code TALYS 1.8 [19].

2 Experimental details

The experiment was performed at the Folded Tandem Ion Accelerator (FOTIA) Facility, Nuclear Physics Division, Bhabha Atomic Research Centre (BARC), Mumbai. Protons of 3 and 4 MeV were bombarded on a 2 mm thick circular LiF pellet target to produce neutrons through the ^{7}Li(p, n)^{7}Be reaction. A fresh LiF pellet target was used for the irradiation at each proton energy. Natural zirconium metal foils of 0.1113 g and 0.2265 g weight were used for the irradiation. The Zr metal foils were wrapped separately with 0.025 mm thick super pure Al foil. Similarly, gold metal foils of 0.0528 g and 0.0623 g weight were also wrapped separately with a 0.025 mm thick Al foil. In each experiment, a zirconium and a gold metal foil were additionally wrapped together with an aluminum foil. The Al wrapped Au-Zr metal foils were mounted at zero-degree angle with respect to the proton beam direction at a distance of 2 mm behind the LiF pellet. The Al wrapped Au-Zr metal foils were irradiated with effective neutron

energies of 0.61 and 1.05 MeV for 8.53 h and 7.75 h, respectively. The gold foils were used for normalization of the measured cross section with the ^{197}Au(n, γ)^{198}Au standard reaction cross section. The irradiated zirconium foils were then cooled for 2.97 h and 2.82 h, respectively. The corresponding gold foils were cooled for 21.76–70.80 h and 42.90–92.28 h, respectively and then mounted separately on different perspex plates. The γ-ray counting of the irradiated foils was performed using a pre-calibrated 105 cm^3 HPGe detector coupled to a PC-based 4094 channel analyzer. The irradiated zirconium and gold samples were kept alternately one at a time at a distance of 1 cm from the end cap of the detector. The resolution of the detector system had a FWHM of 1.8 keV at 1332.5 keV of ^{60}Co.

3 Calculations and data analysis

3.1 Calculation of the average neutron energy

Neutrons were generated from the ^{7}Li(p, n)^{7}Be reaction by using the proton energies of 3 and 4 MeV. The threshold value of the ^{7}Li(p, n) reaction to the ground state of ^{7}Be is 1.881 MeV [20–23]. A second group of neutrons is produced through the ^{7}Li(p, n$_1$)^{7}Be reaction at $E_p \geq 2.37$ MeV in addition to ^{7}Li(p, n$_0$)^{7}Be reaction. The second group of neutrons at lower energies are due to the population of the first excited state of ^{7}Be. The neutron flux energy spectra $\Phi(E)$ from the ^{7}Li(p, n)^{7}Be reaction were calculated by neutron flux energy spectrum code EPEN-Energy of Proton Energy of Neutron [24].

The code EPEN is a deterministic code, which is used for the calculation of the neutron energy spectrum using as neutron source the ^{7}Li(p, n)^{7}Be reaction. This code has been designed for proton energies from the reaction threshold to 7000 keV. The EPEN code studies the thick and thin target ^{7}Li(p, n$_{0,1}$)^{7}Be neutron spectra and it is a user-friendly web interface with which users can calculate neutron spectra without installation. Below the threshold of the three-body breakup reaction, the neutron production is described by the two-body kinematics for ^{7}Li(p, n$_0$)^{7}Be and ^{7}Li(p, n$_1$)^{7}Be reactions. Any combination of the outgoing angle and energy of a neutron (θ, E_n) uniquely specifies the incident energy of protons at the interaction point, which has already been taken care in the EPEN code. EPEN has also been compared with code SimLiT and shows almost perfect agreement for both the (p, n$_0$) and (p, n$_1$) neutron energy spectra for thin and thick lithium targets with and without proton energy spread. The code gives the user the liberty to feed the incident proton energy on the lithium target, the incident proton energy spread, specification of Li foil thickness and geometry, shape and size of the neutron activation sample as well as their distance from the Li foil as input parameters in order to calculate and generate the neutron spectrum for a given initial proton energy. The detailed formalism adopted for the calculation of the neutron spectrum by EPEN is provided by Pachuau *et al.* [24–26].
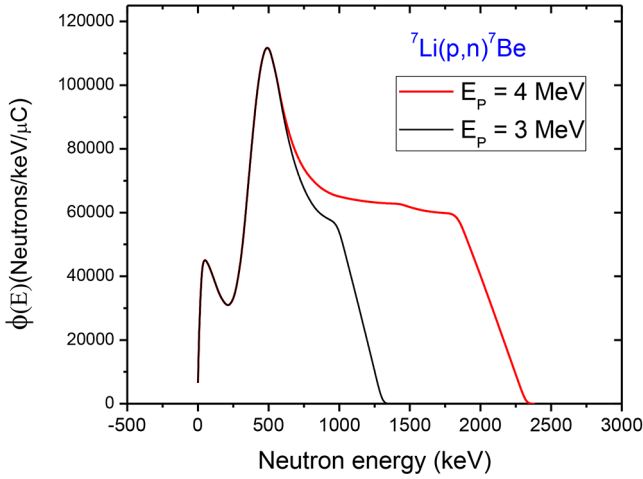
Fig. 1. Neutron flux energy spectra $\Phi(E)$ from the ^{7}Li(p, n) ^{7}Be reactions at $E_p = 3$ and $4\,$MeV obtained from the EPEN code [24].
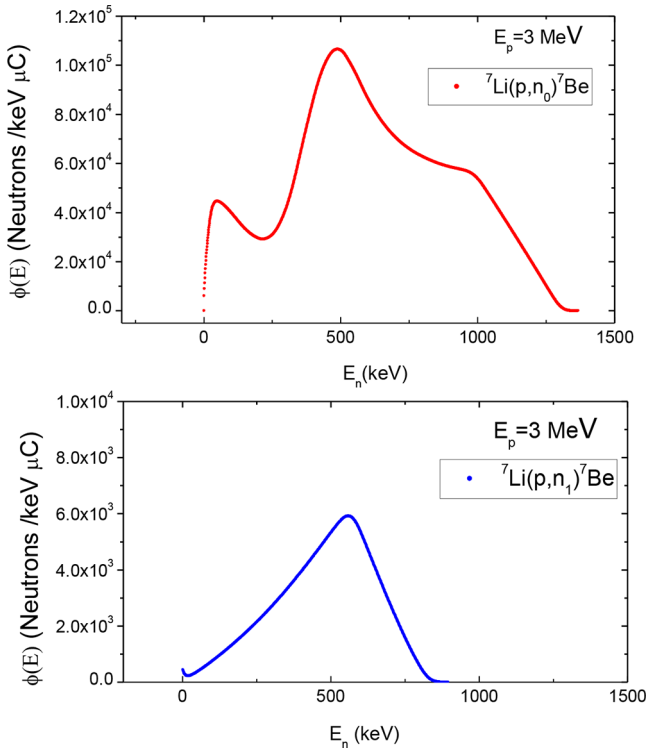

Fig. 2. Neutron flux energy spectra $\phi(E)$ from the ^{7}Li(p, n$_0$)^{7}Be and ^{7}Li(p, n$_1$)^{7}Be reactions at $E_p = 3\,$MeV.

The advantage of using the EPEN code is that the individual (p, n$_0$) and (p, n$_1$) neutron energy spectra can be obtain besides the combined neutron spectrum from both group. However, a limitation of the EPEN code is that the uncertainty in the results based on EPEN is not possible to obtain. The uncertainty in the neutron energy only depends on the uncertainty of proton energy. The total neutron flux energy spectra $\Phi(E)$ calculated by the EPEN code at the two proton energies of the present experimental work are shown in fig. 1. Since both the proton
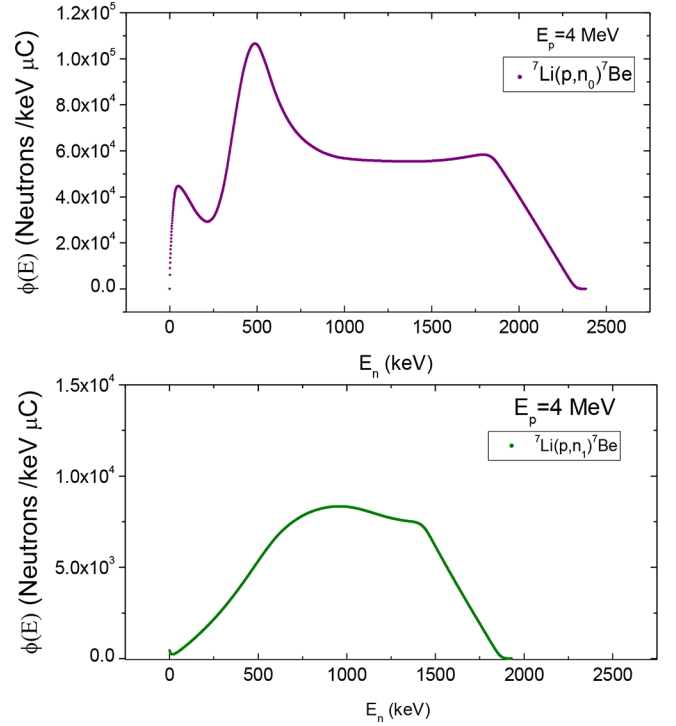

Fig. 3. Neutron flux energy spectra $\phi(E)$ from the ^{7}Li(p, n$_0$)^{7}Be and ^{7}Li(p, n$_1$)^{7}Be reactions at $E_p = 4\,$MeV.

energies in the present experiment are above the threshold energy of ^{7}Li(p, n$_1$)^{7}Be reaction, there is low energy neutrons background from ^{7}Li(p, n$_1$) reaction in addition to the ^{7}Li(p, n$_0$) reaction neutrons as shown in fig. 2 and fig. 3. The mean energy of the ^{7}Li(p, n$_0$) reaction neutron group was obtained from the following relation:

$$\langle E_{\mathrm{n}} \rangle = \frac{\int \Phi_0(E)E\mathrm{d}E}{\int \Phi_0(E)\mathrm{d}E} \,, \tag{1}$$

where $\Phi_0(E)$ is the neutron flux from the ^{7}Li(p, n$_0$)^{7}Be reaction calculated by EPEN (p, n$_0$) neutron flux energy spectra and the corresponding neutron energies are 0.61 and 1.05 MeV for $E_p = 3$ and $4\,$MeV, respectively.

3.2 Efficiency with uncertainty of HPGe detector and its interpolation

The energy and efficiency calibration of the HPGe detector system was carried out by using a standard ^{152}Eu point source ($T_{1/2} = 13.517$ years; source activity (A_0) = 38832 Bq as on 1 October 1999) from their characteristic γ-ray energies [27] retrieved through NuDat 2.7β database [28]. The characteristic γ-ray energies and their corresponding intensities of the ^{152}Eu standard source adopted in the detector efficiency measurement are reported in table 1. The efficiency of the detector was determined from the following equation:

$$\varepsilon_p = \frac{CK_c}{A_0 e^{-\lambda T} I_\gamma \Delta t} \,, \tag{2}$$

Table 1. Detection efficiencies for the point source geometry and for the sample geometry at the characteristic γ-ray energies of ^{152}Eu with γ-ray intensities [25] and coincidence-summing effect correction factors K_c.

Energy (MeV)	γ-ray intensities (%)	Counts, C	K_c	ε_p (efficiency for point source)	ε (efficiency for sample)
0.12178	28.53 ± 0.16	165645 ± 648	1.09745	0.09891	0.086540
0.24470	7.55 ± 0.04	25270 ± 304	1.13450	0.05894	0.051120
0.34428	26.59 ± 0.2	69713 ± 360	1.07470	0.04374	0.037930
0.41112	2.237 ± 0.013	4688 ± 194	1.16977	0.03805	0.033000
0.77890	12.93 ± 0.08	14231 ± 207	1.09953	0.01879	0.016300
0.96406	14.51 ± 0.07	13427 ± 174	1.05610	0.01517	0.013170
1.11208	13.67 ± 0.08	11521 ± 160	1.02343	0.01339	0.011620
1.21295	1.415 ± 0.008	878 ± 65	1.14968	0.01107	0.009609
1.40801	20.87 ± 0.09	13968 ± 132	1.03796	0.01078	0.009359

where C is the detected counts under the photo peak of each γ-line during the counting time Δt, which are given in table 1. The uncertainties in the measured counts C of table 1 are based on the uncertainties given by the software while taking the total number of detected counts under the photo peak. A_0 is the source strength of ^{152}Eu at the time of manufacture, λ ($= \ln 2/T_{1/2}$) is the decay constant for ^{152}Eu, T is the cooling time, *i.e.* the time elapsed between the date of manufacture to the start of counting time. I_γ is the branching intensity or abundance of γ-ray and K_c is the correction factor for the coincidence summing effect.

The count rate from the ^{96}Zr(n, γ)^{97}Zr reaction is low. Hence efficiency calibration of the detector using the standard ^{152}Eu source was performed by placing it at a distance of 1 cm from the detector. However, placing the source at 1 cm distance from the detector end cap introduces a coincidence summing effect [29] and corrections have to be made for the detector efficiency measurement. The correction factor K_c was calculated using the Monte Carlo simulation code EFFTRAN [30,31] where the inputs for the simulation require the specifications of the HPGe detector (*e.g.*, dimension and crystal material, crystal hole cavity, window, end cap, mount cup and absorber) and the ^{152}Eu γ-ray source description (*e.g.*, source dimension, characteristic γ-rays and x-rays). The simulation takes into account the γ-ray–γ-ray, the γ-ray–x-ray and the x-ray–x-ray coincidence and provides the correction factors for the γ-lines at their respective energies.

The efficiency calibration of the HPGe detector obtained for a point source ε_p, using eq. (2) is presented in table 1. However, the irradiated samples in the present experiments have finite dimension, thus, the efficiency obtained for the point source geometry ε_p was transferred to the dimensions of the samples geometry of finite size using EFFTRAN, which are also presented in table 1.

From eq. (2), it can be seen that there are four attributes C, A_0, I_γ and λ that contribute to the uncertainty of the efficiency of the detector. The terms T and Δt are not considered for uncertainty propagation because

uncertainties associated with these terms are considered to be negligible in the present work. The uncertainty in K_c has also been calculated by varying the geometry and was found to be very negligible, so it is not incorporated in the present calculation as it did not bring any difference. The information on the partial errors due to each attributes and their correlations provides a basis for constructing the covariance matrix V_ε [32]. The covariance matrix V_ε was obtained as follows:

$$V_{\varepsilon ij} = \sum_k e_{ik} S_{ijk} e_{jk}, \quad 1 \le i, j \le 9, 1 \le k \le 4, \quad (3)$$

where S_{ijk} is the micro correlation between the i-th observation and j-th observation of the k-th attribute, e_{lk} is the partial uncertainty in efficiency ε_l due to the k-th attribute x_k and is given by

$$e_{lk} = \frac{\partial \varepsilon_l}{\partial x_{lk}} \Delta x_{lk}, \quad 1 \le l \le 9. \quad (4)$$

The micro correlation matrix S_{ijk} for the attributes C and I_γ is an identity matrix I of order 9 as the observations were made independently. However, the micro correlation matrix in the case of the attributes A_0 and λ is a matrix J with all entries equal to 1 and order 9. This is because the same decay constant and same source strength of ^{152}Eu was adopted in the efficiency calculation.

The characteristic γ-ray energies of the radionuclides of interest are different from the characteristic γ-ray energies of ^{152}Eu used in the calibration process. Hence to get the efficiencies at the 743.36 keV and 411.8 keV γ-lines of ^{97}Zr and ^{198}Au, respectively, an appropriate model for interpolation was chosen using the following linear parametric function [32]:

$$\ln \varepsilon_i = \sum_{n=1}^{n=m} p_n (\ln E_i)^{n-1} \quad (5)$$

and the corresponding linear model as $Z \approx AP$ in matrix form, where $Z = \ln(\varepsilon_i)$, ε_i is the efficiency of the detector obtained at γ-ray energies E_i, A is the design matrix

Table 2. The fitting parameters P and the covariance matrix V_P obtained using the model with $n = 4$.

P	V_P			
-4.359	$9.204\text{E}-05$			
-0.968	$-8.161\text{E}-05$	$4.749\text{E}-04$		
0.115	$-2.041\text{E}-04$	$7.137\text{E}-04$	$1.357\text{E}-03$	
0.068	$-7.162\text{E}-05$	$2.230\text{E}-04$	$4.634\text{E}-04$	$1.635\text{E}-04$

with elements $A_{i,n} = (\ln E_i)^{n-1}$ ($1 \le n \le m$; $1 \le i \le 9$). P is a column matrix having elements p_n which are unknown parameters to be estimated and n is the order of the polynomial. The parameter n is varied to achieve the best model for interpolation and the selection was based on minimum Chi-square (χ^2) statistics given by

$$\chi^2 = (Z - AP)^T V_Z^{-1} (Z - AP). \qquad (6)$$

The solution P is obtained by the following formulas [30]:

$$P = V_P A^T V_Z^{-1} Z, \qquad (7)$$

where V_P is the covariance matrix for the solution parameters P, given by

$$V_P = (A^T V_Z^{-1} A)^{-1}. \qquad (8)$$

The matrix V_z in eq. (8) was obtained using $(V_z)_{ij} = (V_\varepsilon)_{ij}/\varepsilon_i \varepsilon_j$. The values of P and V_P were given in table 2. Substituting the solution for P into eq. (6) yields a specific value for χ^2. In the present work, the best fit was obtained for $n = 4$ with $\chi^2/(9-4) = 1.09 \approx 1$ and we consider the corresponding linear parametric model as the best model, which is given by

$$\ln \varepsilon = -4.359 - 0.968 \ln E + 0.115 (\ln E)^2 + 0.068 (\ln E)^3. \qquad (9)$$

Equation (9) is equivalent to

$$\varepsilon = e^{-4.359 - 0.968 \ln E + 0.115 (\ln E)^2 + 0.068 (\ln E)^3}. \qquad (10)$$

The efficiency without coincidence summing correction, the measured efficiencies and the fitted efficiencies obtained are shown in fig. 4. Using the values of P and V_P from table 2, we get the efficiencies along with their correlation for the 743.36 keV and 411.8 keV γ-lines of ^{97}Zr and ^{198}Au, which were presented in table 3.

3.3 Monitor reaction cross section and its uncertainty

In the present work, the ^{197}Au(n,γ)^{198}Au reaction cross section from the IAEA Neutron Cross Section Standards [33] was adopted as the monitor. The reference cross section $\langle \sigma_{\text{Au}} \rangle$ was obtained by folding the point-wise monitor reaction cross section from the IAEA Neutron Cross Section Standards $\sigma_{\text{Au}}(E)$ with the neutron flux energy
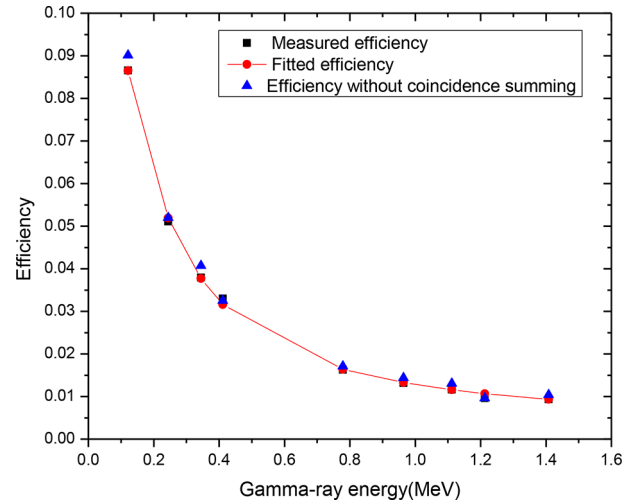

Fig. 4. The efficiency without summing coincidence, the measured and fitted detection efficiency calibration curve of the HPGe detector calibrated at a distance of 1cm from the detector end cap window.

spectrum $\Phi_0(E)$ based on ^{7}Li(p, n$_0$)^{7}Be reaction using the EPEN code [24]

$$\langle \sigma_{\text{Au}} \rangle = \int \sigma_{\text{Au}}(E) \Phi_0(E) \text{d}E \bigg/ \int \Phi_0(E) \text{d}E. \qquad (11)$$

The IAEA Neutron Cross Section Standards provide the covariance information of $\sigma_{\text{Au}}(E)$ for its group-wise cross section [33]. Similarly, the group-wise neutron flux energy spectrum $\Phi_{i,k}$ was also introduced by using the following equation:

$$\Phi_{i,k} = \int_{E_{k,\text{min}}}^{E_{k,\text{max}}} \Phi_i(E) \text{d}E \qquad (12)$$

which satisfies $\sum_k \Phi_{i,k} = 1$, where $i = 1$ for $E_{\text{n}} = 0.61$ MeV and $i = 2$ for $E_{\text{n}} = 1.05$ MeV. For each energy field i, there are k energy groups defined by energy group boundaries in the IAEA Neutron Cross Section Standards. $E_{k,\text{min}}$ and $E_{k,\text{max}}$ are the lower and upper boundaries of the k-th energy group. Then the uncertainty and covariance in the IAEA Neutron Cross Section Standards are propagated to the monitor, $\langle \sigma_{\text{Au}} \rangle$ as given by Otsuka *et al.* [34]

$$(\Delta \langle \sigma_{\text{Au},i} \rangle)^2 = \sum_k \Phi_{i,k}^2 \text{Var}(\langle \sigma_{\text{Au}} \rangle_k)$$
$$+ 2 \sum_{k<l} \Phi_{i,k} \text{Cov}(\langle \sigma_{\text{Au}} \rangle_k, \langle \sigma_{\text{Au}} \rangle_l) \Phi_{i,l}, \quad (13)$$

where $\text{Cov}(\langle \sigma_{\text{Au}} \rangle_k, \langle \sigma_{\text{Au}} \rangle_l)$ and $\text{Var}(\langle \sigma_{\text{Au}} \rangle_k)$ are the covariance between the k-th and the l-th group wise cross sections of ^{197}Au(n,γ)^{198}Au monitor reaction. The summations for k and l are taken for all energy groups between 0.00125 and 1.5 MeV for $i = \langle E_{\text{n}} \rangle = 0.61$ MeV (61 groups), and between 0.00125 and 2.5 MeV for $i = \langle E_{\text{n}} \rangle = 1.05$ MeV (66 groups). The value of the group wise neutron flux energy spectrum $\Phi_{i,k}$ and the IAEA neutron group wise standard cross sections $\langle \sigma_{\text{Au}} \rangle_k$ is summarized

Table 3. Interpolated detector efficiencies and correlation matrix.

Nuclide	Energy (MeV)	Efficiency, ε	Covariance matrix		Correlation matrix	
^{97}Zr	0.74336	0.01719 ± 0.00019	3.6872E $-$ 08		1	
^{198}Au	0.41180	0.03152 ± 0.00028	4.0608E $-$ 08	7.9627E $-$ 08	0.74943	1

in table 4 and plotted in fig. 5. Similarly, the covariance between two spectrum averaged cross sections at 0.61 and 1.05 MeV was obtained by the following equation:

$$\mathrm{Cov}\left(\langle\sigma_{\mathrm{Au},i}\rangle,\langle\sigma_{\mathrm{Au},j}\rangle\right)=\sum_{k,l}\Phi_{i,k}\mathrm{Cov}\left(\langle\sigma_{\mathrm{Au}}\rangle_{k},\langle\sigma_{\mathrm{Au}}\rangle_{l}\right)\Phi_{j,l}.$$
(14)

The correlation coefficients were obtained using the following equation:

$$\mathrm{Cor}\left(\langle\sigma_{\mathrm{Au},i}\rangle,\langle\sigma_{\mathrm{Au},j}\rangle\right)=\frac{\mathrm{Cov}\left(\langle\sigma_{\mathrm{Au},i}\rangle,\langle\sigma_{\mathrm{Au},j}\rangle\right)}{\sqrt{\mathrm{Var}\left(\langle\sigma_{\mathrm{Au},i}\rangle\right)}\times\sqrt{\mathrm{Var}\left(\langle\sigma_{\mathrm{Au},j}\rangle\right)}}.$$
(15)

The correlation coefficients $\mathrm{Cor}(\langle\sigma_i\rangle,\langle\sigma_j\rangle)$ are given in the IAEA Neutron Cross Section Standards [33]. Using eq. (11) and eq. (13) the spectrum averaged monitor cross sections obtained are summarized in table 5 along with the covariance of the spectrum averaged cross sections between the two energies and the correlation matrix.

3.4 ^{96}Zr(n, γ)^{97}Zr reaction cross section and its correction factors

The ^{96}Zr(n, γ)^{97}Zr reaction cross sections at the average neutron energies of 0.61 and 1.05 MeV have been measured relative to the ^{197}Au(n, γ)^{198}Au monitor reaction cross sections. In order to avoid the direct measurement of neutron flux intensity Φ, the cross section of the ^{96}Zr(n, γ)^{97}Zr reaction has been determined using a known monitor standard cross section, $\langle\sigma_{\mathrm{Au}}\rangle$ by the following equation:

$$\langle\sigma_{\mathrm{Zr}}\rangle=\langle\sigma_{\mathrm{Au}}\rangle\frac{C_{\mathrm{Zr}}}{C_{\mathrm{Au}}}\frac{NW_{\mathrm{Au}}a_{\mathrm{Au}}A_{v\mathrm{Zr}}I_{\gamma\mathrm{Au}}\varepsilon_{\mathrm{Au}}f_{\mathrm{Au}}}{NW_{\mathrm{Zr}}a_{\mathrm{Zr}}A_{v\mathrm{Au}}I_{\gamma\mathrm{Zr}}\varepsilon_{\mathrm{Zr}}f_{\mathrm{Zr}}}\times\frac{CF_{\mathrm{Zr}}}{CF_{\mathrm{Au}}}$$
(16)

where $\langle\sigma_{\mathrm{Au}}\rangle$ is the spectrum average ^{197}Au(n, γ)^{198}Au reaction cross section calculated from eq. (11), C_{Zr} and C_{Au} are the photo peak counts for the γ-lines of ^{97}Zr and ^{198}Au, respectively, N is the Avogadro number, W_{Zr} and W_{Au} are the weight of zirconium and gold samples, a_{Zr} and a_{Au} are the isotopic abundance of the respective isotope of ^{96}Zr and ^{197}Au, $A_{v\mathrm{Zr}}$ and $A_{v\mathrm{Au}}$ are the average mass of the element zirconium and gold. The symbols $I_{\gamma\mathrm{Zr}}$, $I_{\gamma\mathrm{Au}}$, $\varepsilon_{\mathrm{Zr}}$, $\varepsilon_{\mathrm{Au}}$, f_{Zr}, f_{Au} are the branching intensity or abundance of γ-ray, efficiencies and time factors of the radioactive nuclide ^{97}Zr and ^{198}Au, respectively. CF_{Zr} and CF_{Au} are the correction factors, which include γ-ray self-attenuation factor, and low energy neutron background correction factor discussed in the following section. The time factor, f_x is defined by

$$f_x=\left[\left(1-e^{-\lambda_x t_{i,x}}\right)e^{-\lambda_x t_{c,x}}\left(1-e^{-\lambda_x t_{m,x}}\right)\right]/\lambda_x,\quad(17)$$

where, t_i, t_c, t_m are the irradiation, cooling and measuring time of the irradiated samples, $x = {}^{97}$Zr or ^{198}Au. The adopted decay data for ^{97}Zr and ^{198}Au have been taken from the ENSDF evaluation [35,36] extracted from the interface of Live Chart of Nuclides of IAEA [37] and are given in table 6.

The correction factor CF_x in eq. (16) is

$$CF_x=CF_{x,\mathrm{low}}\times CF_{x,\mathrm{att}}$$
(18)

where $CF_{x,\mathrm{low}}$ is the low energy neutron background due to ^{7}Li(p, n_1)^{7}Be neutrons and $CF_{x,\mathrm{att}}$ is the γ-ray self-attenuation and $x = $ Zr or Au.

3.4.1 Low-energy background neutron correction factor

Both the proton energies in the present experiment are above the threshold energy of the ^{7}Li(p, n_1)^{7}Be reaction, hence there are (p, n_1) reaction low energy background neutrons in addition to the (p, n_0) reaction neutrons. Subtraction of the (p, n_1) neutron contributions is an essential part in experimental determination of neutron-induced reaction cross section, hence during the analysis of the present measurement the (p, n_1) neutrons contribution can be subtracted and presented by the correction factor,

$$CF_{x,\mathrm{low}}=1-\int\Phi_1\left(E\right)\sigma_x\left(E\right)\mathrm{d}E\left/\int\Phi\left(E\right)\sigma_x\left(E\right)\mathrm{d}E,\right.$$
(19)

as provided by Punte *et al.* [29], where $x = $ Zr or Au, $\Phi_1(E)$ is the (p, n_1) neutron flux energy spectrum generated by EPEN, $\Phi(E)=\Phi_0(E)+\Phi_1(E)$ is the total neutron flux energy spectrum and $\sigma_x(E)$ is the ^{96}Zr(n, γ)^{97}Zr reaction cross section taken from ENDF/B-VIII.0 library [38] or the ^{197}Au(n, γ)^{198}Au reaction cross section taken from IAEA Neutron Cross Sections Standards [33] and the value obtained is reported in table 7.

3.4.2 γ-ray self-attenuation factors

Gamma-ray self-attenuation factor has been calculated due to the interaction of the γ-rays with the foil. This has been done in order to correct the γ-ray spectrometric analysis due to the self-attenuation effect. The attenuation correction factor was obtained using the probability of penetration expression [29,39,40] given as

$$CF_{x,\mathrm{att}}^{-1}=\left[\left(\frac{1}{r_1}\right)\int_0^{r_1}e^{-\mu_{m,1}\rho_1 r}\mathrm{d}r\right]$$
(20)

$$=\left\{\left[1-e^{-\mu_{m,1}\rho_1 r_1}\right]/(\mu_{m,1}\rho_1 r_1)\right\}.$$
(21)

Table 4. Group wise neutron flux energy spectrum $\Phi_{i,k}$ calculated from EPEN code [24] and IAEA Neutron Cross Section Standards [31] group wise cross section with its uncertainties.

Group, k (MeV)	$\langle\sigma_{\mathrm{Au}}\rangle_k$ (mb)	$\langle E_{\mathrm{n}}\rangle = 0.61\,\mathrm{MeV}$	$\langle E_{\mathrm{n}}\rangle = 1.05\,\mathrm{MeV}$
		$\Phi_{i,k}$	$\Phi_{i,k}$
0.00125–0.003	3361.30 ± 603.16	$3.61\mathrm{E}-04$	$2.11\mathrm{E}-04$
0.003–0.004	2627.25 ± 55.14	$3.30\mathrm{E}-04$	$1.93\mathrm{E}-04$
0.004–0.005	2252.09 ± 50.18	$3.84\mathrm{E}-04$	$2.24\mathrm{E}-04$
0.005–0.006	1946.92 ± 28.36	$4.33\mathrm{E}-04$	$2.52\mathrm{E}-04$
0.006–0.007	1714.81 ± 25.71	$4.79\mathrm{E}-04$	$2.80\mathrm{E}-04$
0.007–0.008	1519.60 ± 21.70	$5.23\mathrm{E}-04$	$3.05\mathrm{E}-04$
0.008–0.009	1356.26 ± 20.79	$5.65\mathrm{E}-04$	$3.30\mathrm{E}-04$
0.009–0.01225	1161.64 ± 19.26	$1.64\mathrm{E}-03$	$9.55\mathrm{E}-04$
0.01225–0.0175	907.10 ± 9.95	$2.76\mathrm{E}-03$	$1.61\mathrm{E}-03$
0.0175–0.022	726.36 ± 9.35	$2.75\mathrm{E}-03$	$1.60\mathrm{E}-03$
0.022–0.027	643.77 ± 5.41	$3.07\mathrm{E}-03$	$1.79\mathrm{E}-03$
0.027–0.0375	567.55 ± 3.96	$6.78\mathrm{E}-03$	$3.95\mathrm{E}-03$
0.0375–0.05	480.28 ± 4.28	$8.29\mathrm{E}-03$	$4.84\mathrm{E}-03$
0.05–0.06	423.45 ± 4.00	$6.54\mathrm{E}-03$	$3.81\mathrm{E}-03$
0.06–0.07	390.66 ± 3.65	$6.44\mathrm{E}-03$	$3.76\mathrm{E}-03$
0.07–0.08	363.19 ± 3.46	$6.30\mathrm{E}-03$	$3.68\mathrm{E}-03$
0.08–0.09	339.46 ± 3.34	$6.14\mathrm{E}-03$	$3.58\mathrm{E}-03$
0.09–0.0975	325.18 ± 3.18	$4.90\mathrm{E}-03$	$2.86\mathrm{E}-03$
0.0975–0.11	313.94 ± 3.19	$7.39\mathrm{E}-03$	$4.31\mathrm{E}-03$
0.11–0.135	295.55 ± 2.82	$1.28\mathrm{E}-02$	$7.49\mathrm{E}-03$
0.135–0.16	277.44 ± 2.75	$1.17\mathrm{E}-02$	$6.85\mathrm{E}-03$
0.16–0.175	267.33 ± 3.05	$6.79\mathrm{E}-03$	$3.96\mathrm{E}-03$
0.175–0.185	262.09 ± 6.02	$4.52\mathrm{E}-03$	$2.63\mathrm{E}-03$
0.185–0.195	257.32 ± 3.48	$4.42\mathrm{E}-03$	$2.58\mathrm{E}-03$
0.195–0.205	252.82 ± 3.54	$4.34\mathrm{E}-03$	$2.53\mathrm{E}-03$
0.205–0.215	249.30 ± 3.22	$4.30\mathrm{E}-03$	$2.50\mathrm{E}-03$
0.215–0.225	246.56 ± 3.24	$4.29\mathrm{E}-03$	$2.50\mathrm{E}-03$
0.225–0.2325	243.38 ± 3.84	$3.54\mathrm{E}-03$	$2.07\mathrm{E}-03$
0.2325–0.2375	239.37 ± 3.08	$2.78\mathrm{E}-03$	$1.62\mathrm{E}-03$
0.2375–0.2425	236.92 ± 4.34	$2.81\mathrm{E}-03$	$1.64\mathrm{E}-03$
0.2425–0.2475	236.68 ± 3.00	$2.85\mathrm{E}-03$	$1.66\mathrm{E}-03$
0.2475–0.255	236.70 ± 3.27	$3.74\mathrm{E}-03$	$2.18\mathrm{E}-03$
0.255–0.265	235.11 ± 3.08	$4.74\mathrm{E}-03$	$2.76\mathrm{E}-03$
0.265–0.275	229.01 ± 3.74	$4.99\mathrm{E}-03$	$2.91\mathrm{E}-03$
0.275–0.29	215.98 ± 2.78	$7.85\mathrm{E}-03$	$4.58\mathrm{E}-03$
0.29–0.3125	200.52 ± 2.34	$1.35\mathrm{E}-02$	$7.87\mathrm{E}-03$
0.3125–0.3375	188.51 ± 2.17	$1.84\mathrm{E}-02$	$1.07\mathrm{E}-02$
0.3375–0.3625	178.83 ± 1.91	$2.26\mathrm{E}-02$	$1.32\mathrm{E}-02$
0.3625–0.3875	169.90 ± 1.78	$2.69\mathrm{E}-02$	$1.57\mathrm{E}-02$
0.3875–0.4125	162.33 ± 1.67	$3.09\mathrm{E}-02$	$1.80\mathrm{E}-02$
0.4125–0.4375	154.74 ± 1.83	$3.44\mathrm{E}-02$	$2.00\mathrm{E}-02$
0.4375–0.4625	147.23 ± 1.47	$3.68\mathrm{E}-02$	$2.15\mathrm{E}-02$

Table 4. Continued.

Group, k (MeV)	$\langle\sigma_{\mathrm{Au}}\rangle_k$ (mb)	$\langle E_{\mathrm{n}}\rangle = 0.61\,\mathrm{MeV}$	$\langle E_{\mathrm{n}}\rangle = 1.05\,\mathrm{MeV}$
		$\Phi_{i,k}$	$\Phi_{i,k}$
0.4625–0.4875	141.56 ± 1.50	3.81E − 02	2.22E − 02
0.4875–0.51	136.44 ± 1.43	3.40E − 02	1.98E − 02
0.51–0.53	130.49 ± 1.44	2.90E − 02	1.69E − 02
0.53–0.555	124.82 ± 1.47	3.45E − 02	2.01E − 02
0.555–0.585	118.42 ± 1.79	3.86E − 02	2.25E − 02
0.585–0.625	109.56 ± 1.18	4.67E − 02	2.73E − 02
0.625–0.675	101.19 ± 1.28	5.27E − 02	3.07E − 02
0.675–0.725	96.50 ± 1.09	4.82E − 02	2.81E − 02
0.725–0.775	93.31 ± 1.21	4.50E − 02	2.62E − 02
0.775–0.825	89.21 ± 0.93	4.28E − 02	2.49E − 02
0.825–0.875	85.91 ± 1.40	4.11E − 02	2.40E − 02
0.875–0.92	84.91 ± 1.85	3.60E − 02	2.10E − 02
0.92–0.95	85.10 ± 1.64	2.39E − 02	1.39E − 02
0.95–0.97	85.36 ± 3.62	1.60E − 02	9.36E − 03
0.97–0.99	84.13 ± 2.67	1.56E − 02	9.31E − 03
0.99–1.05	80.89 ± 0.84	4.13E − 02	2.69E − 02
1.05–1.175	77.43 ± 1.08	5.88E − 02	5.49E − 02
1.175–1.325	74.13 ± 0.94	2.16E − 02	6.53E − 02
1.325–1.5	70.96 ± 1.22	4.68E − 05	7.59E − 02
1.5–1.7	66.75 ± 1.01		8.81E − 02
1.7–1.9	60.18 ± 1.23		8.93E − 02
1.9–2.1	52.34 ± 0.86		6.27E − 02
2.1–2.3	44.16 ± 0.82		2.41E − 02
2.3–2.5	37.09 ± 0.83		4.61E − 04
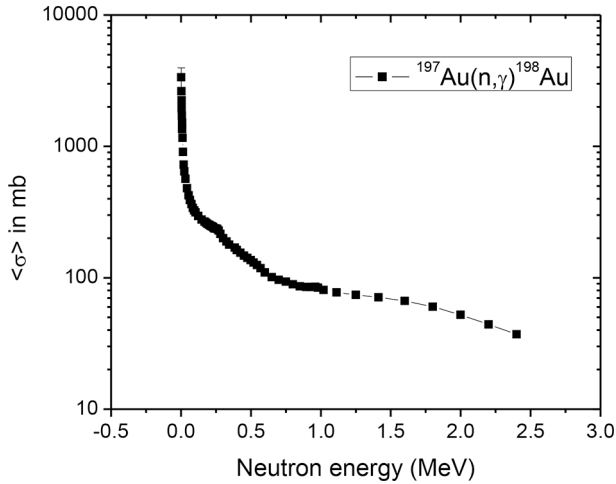
Fig. 5. The IAEA neutron group wise standard cross sections ($\langle\sigma_{\mathrm{Au}}\rangle$) of $^{197}\mathrm{Au}(\mathrm{n},\gamma)^{198}\mathrm{Au}$ reaction [31] as a function of average neutron energy range.

The foil of thickness r_1 having volume mass density ρ_1 is the source of the γ-line detected by the detector. $\mu_{m,1}$ is the mass attenuation coefficient of the γ-ray energy and material calculated by XMuDatVer 1.01 [41]. The correction factor obtained is given in table 7.

4 Uncertainty in cross section measurement

The $^{96}\mathrm{Zr}(\mathrm{n},\gamma)^{97}\mathrm{Zr}$ reaction cross sections have been determined by using eq. (16) at effective neutron energies of $\langle E_{\mathrm{n}}\rangle = 0.61\,\mathrm{MeV}$ and $\langle E_{\mathrm{n}}\rangle = 1.05\,\mathrm{MeV}$. At both neutron energies, the $^{96}\mathrm{Zr}(\mathrm{n},\gamma)^{97}\mathrm{Zr}$ reaction cross section was measured with reference to the $^{197}\mathrm{Au}(\mathrm{n},\gamma)^{198}\mathrm{Au}$ monitor reaction. The same detector efficiency model was used in the efficiency interpolation of the characteristic γ-ray energies of $^{97}\mathrm{Zr}$ (743.36 keV) and $^{198}\mathrm{Au}$ (411.8 keV) at $\langle E_{\mathrm{n}}\rangle = 0.61\,\mathrm{MeV}$ and $\langle E_{\mathrm{n}}\rangle = 1.05\,\mathrm{MeV}$, respectively. As seen from eq. (16) the attributes observed with errors are counts ($C_{\mathrm{Zr}}, C_{\mathrm{Au}}$), weight ($W_{\mathrm{Zr}}, W_{\mathrm{Au}}$), isotopic abundance ($a_{\mathrm{Zr}}$), average mass ($A_{v,\mathrm{Zr}}, A_{v,\mathrm{Au}}$), γ-ray intensity ($I_{\gamma\mathrm{Zr}}, I_{\gamma\mathrm{Au}}$), efficiency ($\varepsilon_{\mathrm{Zr}}, \varepsilon_{\mathrm{Au}}$), the spectrum averaged monitor cross section, $\langle\sigma_{\mathrm{Au}}\rangle$, the low energy neutron background ($CF_{x,\mathrm{low\ Zr}}, CF_{x,\mathrm{Au}}$) and the time factor ($f_{\mathrm{Zr}}, f_{\mathrm{Au}}$) related to decay constant λ. Thus, the covariance information related to the two measured cross sections of the $^{96}\mathrm{Zr}(\mathrm{n},\gamma)^{97}\mathrm{Zr}$ reaction at 0.61 MeV and 1.05 MeV is given in a 2×2 covariance matrix $V_{\sigma\mathrm{Zr}}$ obtained using the following relation:

$$(V_{\sigma\mathrm{Zr}})_{ij} = \sum_{kl}(e_k)_i\,(S_{kl})_{ij}\,(e_l)_j, \qquad 1 \le i,j \le 2,$$

$$1 \le k,l \le 16, \quad (22)$$

Table 5. Spectrum averaged monitor cross section, its uncertainty and correlation matrix.

i	$\langle E_n \rangle$ (MeV)	$\langle \sigma_{Au} \rangle$ mb	Covariance matrix		Correlation matrix	
1	0.61	148.88 ± 0.85	0.72		1	
2	1.05	112.72 ± 0.65	0.51	0.43	0.93	1

Table 6. Decay data for the assessed radionuclides evaluated in the ENSDF library [33,34] as extracted from the interface of Live Chart of nuclides of IAEA [35].

Reaction	Nuclide	Spin state, J^π	Half-life	Decay mode	γ-energy (keV)	γ-ray intensity (%)
^{96}Zr$(n,\gamma)^{97}$Zr	^{97}Zr	$1/2^+$	16.749 ± 0.008 h	β^- (100%)	743.36	93.09 ± 0.16
^{197}Au$(n,\gamma)^{198}$Au	^{198}Au	2^-	2.6941 ± 0.0002 d	β^- (100%)	411.80	95.62 ± 0.06

Table 7. Correction factors due to low energy background neutrons ($CF_{x,\mathrm{low}}$) and γ-ray self-attenuation ($CF_{x,\mathrm{att}}$) applied to the measured cross section.

Correction factors	Neutron energy, E_n (MeV)	
	0.61	1.09
$C_{f\mathrm{Zr,low}}$	0.972 ± 0.005	0.925 ± 0.017
$C_{f\mathrm{Au,low}}$	0.967 ± 0.0002	0.936 ± 0.0004
$C_{f\mathrm{Zr,att}}$	1.006	1.007
$C_{f\mathrm{Au,att}}$	1.012	1.014

where $(S_{kl})_{ij}$ represents the correlation between the k-th attribute in the i-th experimental observation and l-th attribute in the j-th experimental observation and is called micro-correlation, $(e_k)_i = \frac{\partial \sigma_{\mathrm{Zr}i}}{\partial (x_k)_i} \Delta(x_k)_i$ is the partial uncertainty in $\langle \sigma_{\mathrm{Zr}} \rangle_i$ due to the k-th attribute in the i-th experimental observation and $(e_l)_j = \frac{\partial \sigma_{\mathrm{Zr}j}}{\partial (x_l)_j} \Delta(x_l)_j$ is the partial uncertainty in $\langle \sigma_{\mathrm{Zr}} \rangle_j$ due to the l-th attribute in the j-th experimental observation [42–44]. Since the uncertainties in the parameters t_i, t_c and t_m have been considered negligible in the present experiment, the only attribute that contributes to the uncertainty in the time factor f is the decay constant, λ. The uncertainties in the time factors were propagated from the uncertainties in the decay constants [34], given by

$$(\Delta f / f)^2 = s_{f\lambda}^2 (\Delta \lambda / \lambda)^2, \tag{23}$$

$f = f_{\mathrm{Zr}}$ or f_{Au} and $\lambda = \lambda_{\mathrm{Zr}}$ or λ_{Au} with relative sensitivity $s_{f\lambda}$,

$$s_{f\lambda} = \frac{\lambda}{f} \frac{\partial f}{\partial \lambda} = \left(\frac{\lambda t_i e^{-\lambda t_i}}{1 - e^{-\lambda t_i}} - \lambda t_c + \frac{\lambda t_m e^{-\lambda t_m}}{1 - e^{-\lambda t_m}} - 1 \right). \tag{24}$$

The uncertainty in decay constant, $\Delta \lambda = \frac{\ln 2 \Delta T_{1/2}}{T_{1/2}^2}$ where $T_{1/2}$ was taken from the ENSDF evaluation extracted from the interface of Live Chart of Nuclides of IAEA [35–37].

The partial uncertainties due to the various attributes involved in the cross section measurement of the ^{96}Zr$(n,\gamma)^{97}$Zr reaction relative to ^{197}Au$(n,\gamma)^{198}$Au monitor reaction are summarized in table 8. We have used the expression $e_k = \frac{\partial \sigma_{\mathrm{Zr}}}{\partial (x_k)} \Delta(x_k)$, to find the partial uncertainty e_k in σ_{Zr} due to attribute x_k. For instance the value $8.276\mathrm{E}-01$ presented in the second column of table 8 is the partial uncertainty in the measurement of the ^{96}Zr$(n,\gamma)^{97}$Zr reaction cross section due to γ-ray peak counts, which was obtained by taking the partial derivative of the expression given in eq. (16) with respect to γ-ray peak counts C_{Zr}

$$\frac{\partial}{\partial C_{\mathrm{Zr}}} \left(\langle \sigma_{\mathrm{Au}} \rangle \frac{C_{\mathrm{Zr}}}{C_{\mathrm{Au}}} \frac{N W_{\mathrm{Au}} a_{\mathrm{Au}} A_{v\mathrm{Zr}} I_{\gamma\mathrm{Au}} \varepsilon_{\mathrm{Au}} f_{\mathrm{Au}} CF_{\mathrm{Zr}}}{N W_{\mathrm{Zr}} a_{\mathrm{Zr}} A_{v\mathrm{Au}} I_{\gamma\mathrm{Zr}} \varepsilon_{\mathrm{Zr}} f_{\mathrm{Zr}} CF_{\mathrm{Au}}} \right)$$
$$\times \Delta C_{\mathrm{Zr}} = \frac{\Delta C_{\mathrm{Zr}}}{C_{\mathrm{Zr}}} \langle \sigma_{\mathrm{Zr}} \rangle \tag{25}$$

and by considering the rest of the other attributes as constant. The micro-correlations are assigned for each attribute. The last column of table 8 explains the correlations that exist between the two observations. The counts and weights of Zr and Au, respectively, were measured independently and thus the attributes, counts and weights are uncorrelated. The micro-correlation matrices associated within the attributes a_{Zr}, $A_{v\mathrm{Zr}}$, $A_{v\mathrm{Au}}$, $I_{\gamma\mathrm{Zr}}$, and $I_{\gamma\mathrm{Au}}$ are fully correlated, as the same observations of attributes were used in both the experiments. The measurements of $\langle \sigma_{\mathrm{Au}} \rangle$ corresponding to both the neutron fields is partially correlated with correlation coefficient 0.93. There exists a micro-correlation between $\varepsilon_{\mathrm{Zr}}$ and $\varepsilon_{\mathrm{Au}}$ with reference to the same characteristic γ-lines and they are thus fully correlated. However, there exists a partial correlation coefficient between $\varepsilon_{\mathrm{Zr}}$ and $\varepsilon_{\mathrm{Au}}$ since the same efficiency interpolation model was used in both experiments and the partial correlation coefficient was 0.74943. The final covariance in the cross section was constructed by substituting the partial uncertainties data and the corresponding micro-correlation in eq. (22). The result of the measured ^{96}Zr$(n,\gamma)^{97}$Zr reaction cross section along with its uncertainty is presented in table 9.

Table 8. Partial uncertainties and correlations from various attributes involved in the measurement of ^{96}Zr(n,γ)^{97}Zr reaction cross section relative to the ^{197}Au(n,γ)^{198}Au monitor reaction cross section.

Attributes	$\langle E_n \rangle = 0.61$ MeV	$\langle E_n \rangle = 1.05$ MeV	Correlations
γ-ray peak counts, C_{Zr}	8.276E − 01	4.122E − 01	uncorrelated
γ-ray peak counts, C_{Au}	6.251E − 01	5.296E − 01	uncorrelated
Isotopic abundance, a_{Zr}	2.161E − 01	2.559E − 01	fully correlated
Weight, W_{Au}	1.401E − 01	1.661E − 01	uncorrelated
Weight, W_{Zr}	1.329E − 01	1.582E − 01	uncorrelated
Efficiency, $\varepsilon_{Zr}{}^b$	7.511E − 02	8.892E − 02	fully correlated
Efficiency, $\varepsilon_{Au}{}^c$	6.020E − 02	7.127E − 02	fully correlated
Monitor reaction cross section, $\langle \sigma_{Au} \rangle$	3.823E − 02	4.620E − 02	partially correlated^a
Low-energy neutron background correction factor, $C_{x,\text{low},Zr}$	3.726E − 02	1.435E − 01	partially correlated
γ-ray abundance, $I_{\gamma,Zr}$	1.156E − 02	1.368E − 02	fully correlated
γ-ray abundance, $I_{\gamma,Au}$	4.219E − 03	4.996E − 03	fully correlated
Time factor, f_{Zr}	1.538E − 03	1.892E − 03	fully correlated
Low-energy neutron background correction factor, $C_{x,\text{low},Au}$	1.581E − 03	3.530E − 03	partially correlated
Average mass, $A_{v,Zr}$	1.474E − 04	1.745E − 04	fully correlated
Average mass, $A_{v,Au}$	1.366E − 07	1.617E − 07	fully correlated
Time factor, f_{Au}	9.183E − 05	2.569E − 05	fully correlated

^{a} Partial correlation coefficient 0.93 (table 5).
^{b,c} A partial correlation exists between ε_{Zr} and ε_{Au} with partial correlation coefficient 0.74943 (table 3).

Table 9. The experimentally determined ^{96}Zr(n,γ)^{97}Zr reaction cross section ($\langle \sigma_{Zr} \rangle$) along with its uncertainty.

Neutron energy, $\langle E_n \rangle$ MeV	^{96}Zr(n,γ)^{97}Zr reaction cross section, $\langle \sigma_{Zr} \rangle$ (mb)	Covariance matrix		Correlation matrix	
0.61	6.72 ± 1.09	1.18		1.0	
1.05	7.96 ± 0.78	0.08	0.61	0.10	1.0

5 Results and discussions

The spectrum averaged ^{96}Zr(n,γ)^{97}Zr reaction cross section ($\langle \sigma_{Zr} \rangle$) relative to the ^{197}Au(n,γ)^{198}Au monitor reaction has been measured using the activation and off-line γ-ray spectrometry technique at the effective neutron energies of 0.61 MeV and 1.05 MeV. The experimentally determined ^{96}Zr(n,γ)^{97}Zr reaction cross sections along with their uncertainties are reported in table 9. For comparison, the excitation function of the ^{96}Zr(n,γ)^{97}Zr reaction as a function of neutron energy from 0.1 to 2.5 MeV has been calculated using the computer code TALYS 1.8 [19]. The back-shifted Fermi gas model with varying level density parameter and Brink-Axel Lorentzian γ-ray strength function was adopted. An excellent agreement between the calculated and experimental ^{96}Zr(n,γ)^{97}Zr reaction cross sections data was obtained by adjusting the level density parameter, $a = 8.94$ with the shell damping factor, $\gamma = 0.27$. The adjusted normalization factor for gamma-

ray transmission coefficient is, $g_{\text{norm}} = 2$. The theoretical calculations have been performed using the default parameter values except for the level-density models and γ-ray strength functions.

The experimental ^{96}Zr(n,γ)^{97}Zr reaction cross sections at the neutron energies of 0.61 and 1.05 MeV from the present work and the theoretical values from TALYS-1.8 code [19], TENDL-2015 data library [45] as well as the evaluated data from CENDL-3.1 [46], JENDL-4.0 [47], JEFF-3.3 [48], and ENDF/B-VIII.0 [38] as a function of neutron energy are plotted in fig. 6. It can be seen from fig. 6 that the present data at the neutron energies of 0.61 and 1.05 MeV are in excellent agreement with the theoretical values from the TALYS-1.8 code [19]. Similarly, the present data are also in agreement with the value from TENDL-2015 library [44] only at the neutron energy of 1.05 MeV but not at 0.61 MeV. Besides this, the present datum at the neutron energy of 0.61 MeV is also in close

Table 10. The experimentally determined $^{96}Zr(n,\gamma)^{97}Zr$ reaction cross section ($\langle\sigma_{Zr}\rangle$) along with the evaluated cross sections, folded by the $^7Li(p,n_0)$ reaction neutron flux energy spectra for TALYS-1.8 [19], TENDL-2015 [45], CENDL-3.1 [46], JENDL-4.0 [47], JEFF-3.3 [48], and ENDF/B-VIII.0 [38] libraries.

	$^{96}Zr(n,\gamma)^{97}Zr$ Reaction Cross section $\langle\sigma_{Zr}\rangle$ (mb)						
Energy (MeV)	Present work	TALYS 1.8	TENDL-2015	CENDL-3.1	JENDL-4.0	JEFF-3.3	ENDF/B-VIII.0
0.61	6.72 ± 1.09	7.72	6.59	6.29	7.89	8.56	7.76
1.05	7.96 ± 0.78	8.50	8.72	7.94	10.35	11.39	10.30
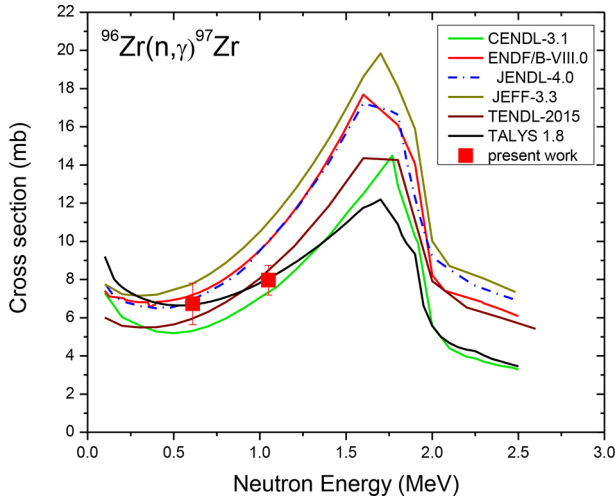
Fig. 6. Plot of the experimentally measured spectrum averaged $^{96}Zr(n,\gamma)^{97}Zr$ reaction cross sections along with the calculated values from TALYS-1.8 [19] and TALYS based TENDL-2015 [44] data library as well as the evaluated data from CENDL-3.1 [45], JENDL-4.0 [46], JEFF-3.3 [47] and ENDF/B-VIII.0 [36] libraries as a function of neutron energy.

agreement only with the evaluated data of JENDL-4.0 [46] and ENDF/B-VIII.0 [38] libraries but not with the other evaluated data libraries.

In order to examine the above discrepancy, the calculated and all the evaluated cross sections of the $^{96}Zr(n,\gamma)^{97}Zr$ reaction have been folded by the $^7Li(p,n_0)$ reaction neutron flux energy spectra from the EPEN code [24]. In table 10, the experimentally determined $^{96}Zr(n,\gamma)^{97}Zr$ reaction cross sections ($\langle\sigma_{Zr}\rangle$) from the present work were compared with the spectrum folded theoretical values from TALYS 1.8 and TENDL-2015 [45] library as well as with the evaluated values from the CENDL-3.1 [46], JENDL-4.0 [47], JEFF-3.3 [48], and ENDF/B-VIII.0 [38] library. As seen from table 10, the experimentally measured cross sections at the average neutron energy of 0.61 MeV, within the uncertainty limit are in agreement with the spectrum folded theoretical value from TALYS-1.8 and TENDL-2015 library [45] as well as with the evaluated data of different libraries [38, 46–48]. On the other hand, at the neutron energy of 1.05 MeV, the present datum within uncertainty limit is in agreement with the spectrum folded theoretical value from TALYS-1.8, TENDL-2015 [45] library and evaluated data of CENDL-3.1 [46] library but not with other libraries [38, 47, 48].

From the above discussion it is clear how experimental data are useful in testing theoretical model and different evaluation. This also implies that it is very much necessary to choose proper parameters for the theoretical model used in TALYS calculation. However, the primary importance of the $^{96}Zr(n,\gamma)^{97}Zr$ reaction cross sections is their applications in the design of the conventional and advanced reactors, where zirconium and its alloy such as zircaloy are used as accessory structural materials and cladding material of fuel.

6 Summary

The $^{96}Zr(n,\gamma)^{97}Zr$ reaction cross sections relative to the $^{197}Au(n,\gamma)^{198}Au$ monitor reaction at the neutron energies of 0.61 and 1.05 MeV have been measured for the first time. The neutron beams have been generated by using the $^7Li(p,n)^7Be$ reaction with the proton energies of 3 and 4 MeV. The data analysis is carried out using the latest decay data and by making the necessary corrections resulting from the contribution of the low energy $^7Li(p,n_1)$ reaction neutron backgrounds, and γ-ray self-attenuation. Covariance analysis has also been carried out to determine the uncertainty in the measured cross section. The present data at the neutron energies of 0.61 and 1.05 MeV were found to be in excellent agreement with the theoretical values from TALYS-1.8 code with the back-shifted Fermi gas model and Brink-Axel Lorentzian γ-ray strength functions. The theoretical values of TALYS-1.8 and TENDL-2015 as well as the evaluated data of CENDL-3.1, JENDL-4.0, JEFF-3.3, and ENDF/B-VIII.0 libraries have been folded by using the $^7Li(p,n_0)$ reaction neutron flux energy spectra from the EPEN code. At the neutron energy of 0.61 MeV, the present datum within uncertainty limit is in agreement with the spectrum folded theoretical data of TALYS-1.8 and the evaluated data of nuclear data libraries [38, 46–48]. At the neutron energy of 1.05 MeV, the present datum within uncertainty limit is also in agreement with the spectrum folded theoretical data of TALYS-1.8 and TENDL-2015 library as well as with the evaluated data of CENDL-3.1 library but not with those of JENDL-4.0, JEFF-3.3 and ENDF/B-VIII.0 libraries.

References

1. F. Carminati, R. Klapisch, J.P. Revol, J.A. Rubio, C. Rubia, CERN/AT/93-49(ET) (1993).
2. C. Rubia, J.A. Rubio, S. Buono, F. Carminati, N. Fietier, J. Galvez, C. Geles, Y. Kadi, R. Klapisch, P. Man-drilion, J.P. Revol, Ch. Roche, CERN/LHC/97-01(EET) (1997).
3. C.D. Bowman, Annu. Rev. Nucl. Part. Sci. **48**, 505 (1998).
4. R.A. Forrest, J. Kopecky, J.C. Sublet, J. Nucl. Sci. Technol. **39**, 96 (2014).
5. DOE Fundamentals handbook material science, DOE-HDBK-1017/2-93 January, Vol. **2** (U.S. Department of Energy FSC-6910 Washington, D.C. 20585, 1993).
6. R.H. Zee, M.W. Guinan, J.S. Huang, J. Nucl. Mater. **141-143**, 874 (1986).
7. N. Stojilovic, E.T. Bender, R.D. Ramsier, Prog. Surface Sci. **78**, 101 (2005).
8. *IAEA Delayed hydride cracking in zirconium alloys in pressure tube nuclear reactors*, final report of a coordinated research project: IAEA TECDOC-1410, available online at `http://www-nds.iaea.org`.
9. G.R. Pansare, P.M. Dighe, V.N. Bhoraskar, Rad. Phys. Chem. **40**, 213 (1992).
10. P. Patnaik, *Handbook of Inorganic Chemicals* (McGraw-Hill, 2003) p. 995.
11. L.L. Shreir, R.A. Jarman, G.T. Burstein, *Corrosion, Third Edition*, Vol. **1** (Butterworth-Heinemann, Oxford, 1994).
12. P. Rudling, A. Strasser, F. Garzarolli, *IZNA7 Special topic report welding of zirconium alloys*, reviewed by Leo van Swam Richland, WA, USA, Advanced Nuclear Technology International Krongjutarvagen 2C, SE-73 0 50 Skultuna Sweden (2007).
13. M. Tessler, M. Paul, A. Arenshtam, G. Feinberg, M. Friedman, S. Halfon, D. Kijel, L. Weissman, O. Aviv, D. Berkovits, Y. Eisen, I. Eliyahu, G. Haquin, A. Kreisel, I. Mardor, G. Shimel, A. Shor, I. Silverman, Z. Yungrais, Phys. Lett. B **751**, 418 (2015).
14. K.S. Krane, J. App. Radiat. Isot. **94**, 60 (2014).
15. P.M. Prajapati, S. Mukherjee, H. Naik, A. Goswami, S.V. Suryanarayana, S.C. Sharma, B.S. Shivashankar, V.K. Mulik, K.C. Jagdeesan, S.V. Thakre, S. Bisnoi, T. Patel, K.K. Rasheed, S. Ganesan, Nucl. Sci. Eng. **171**, 78 (2012).
16. R.E. Heft, in *Conference on Computers in Active Analysis, Mayaguez*, 78MAYAG (1978) p. 495.
17. IAEA-EXFOR database available at `http://www-nds.iaea.org/exfor`.
18. N. Otuka, E. Dupont, V. Semkova, B. Pritychenko, A.I. Blokhin, M. Aikawa, S. Babykina, M. Bossant, G. Chen, S. Dunaeva, R.A. Forrest, T. Fukahori, N. Furutachi, S. Ganesan, Z. Ge, O.O. Gritzay, M. Herman, S. Hlavač, K. Katō, B. Lalremruata, Y.O. Lee, A. Makinaga, K. Matsumoto, M. Mikhaylyukova, G. Pikulina, V.G. Pronyaev,

19. A. Saxena, O. Schwerer, S.P. Simakov, N. Soppera, R. Suzuki, S. Takács, X. Tao, S. Taova, F. Tárkányi, V.V. Varlamov, J. Wang, S.C. Yang, V. Zerkin, Y. Zhuang, Nucl. Data Sheets **120**, 272 (2014).
19. A.J. Koning, S. Hilaire, S. Goriely, *TALYS User Manual: A Nuclear Reaction Program* (ZG Petten, The Netherlands, 2015).
20. H. Liskien, A. Paulsen, At Data Nucl. Data Tables **15**, 57 (1975).
21. C.H. Poppe, J.D. Anderson, J.C. Davis, C. Grimes, C. Wong, Phys. Rev. C **14**, 438 (1976).
22. J.W. Meadows, D.L. Smith, Argon National Laboratory Report ANL-7983, 919720 (1972).
23. S.G. Mashnik, M.B. Chadwick, H.G. Hughes, R.C. Little, R.E. MacFarlane, L.S. Waters, P.G. Young, $^7Li(p, n)$ *Nuclear Data Library for Incident Proton Energies to 150 MeV*, Los Alamos National Laboratory, Los Alamos, NM 87545, USA (2008).
24. R. Pachuau, B. Lalremruata, N. Otuka, L.R. Hlondo, L.R.M. Punte, H.H. Thanga, Nucl. Sci. Eng. **187**, 70 (2017) `http://www.nhergmzu.com/epen/`.
25. Rebecca Pachuau, B. Lalremruata, N. Otuka, L.R. Hlondo, L.R.M. Punte, H.H. Thanga, EPJ Web of Conferences **146**, 12016 (2017).
26. B. Lalremruata, L.R.M. Punte, N. Otuka, R. Pachuau, Y. Iwamoto, S.V. Suryanarayana, B.K. Nayak, B. Satheesh, H.H. Thanga, L.S. Danu, V.V. Desai, L.R. Hlondo, S. Kailas, S. Ganesan, A. Saxena, *Measurements of neutron capture cross sections on 70 Zn at 0.96 and 1.69 MeV*, INDC (IND)-0049 (IAEA, 2017).
27. M.J. Martin, Nucl. Data Sheets **114**, 1497 (2013).
28. National Nuclear Data Center, Brookhaven National Laboratory, `http://www.nndc.bnl.gov/`.
29. L.R.M. Punte, B. Lalremruata, N. Otuka, S.V. Suryanarayana, Y. Iwamoto, R. Pachuau, B. Satheesh, H.H. Thanga, L.S. Danu, V.V. Desai, L.R. Hlondo, S. Kailas, S. Ganesan, B.K. Nayak, A. Saxena, Phys. Rev. C **95**, 024619 (2017).
30. T. Vidmar, Nucl. Instrum. Methods Phys. Res. Sect. A **550**, 603 (2005).
31. T. Vidmar, Gunter Kanisch, GajVidmar, App. Radiat. Isot. **69**, 908 (2011).
32. L.P. Geraldo, D.L. Smith, Nucl. Instrum. Methods Phys. Res. A **290**, 499 (1990).
33. A.D. Carlson, V.G. Pronyaev, D.L. Smith, N.M. Larson, Z. Chen, G.M. Hale, F.J. Hambsch, E.V. Gai, S.-Y. Oh, S.A. Badikov, T. Kawano, H.M. Hofmann, H. Vonach, S. Tagesen, Nucl. Data Sheets **110**, 3215 (2009).
34. N. Otsuka, B. Lalremruata, M.U. Khandaker, A.R. Usman, L.R.M. Punte, Radiat. Phys. Chem. **140**, 502 (2017).
35. N. Nica, Nucl. Data Sheets **111**, 525 (2010).
36. H. Xiaolong, K. Mengxiao, Nucl. Data Sheets **133**, 221 (2016).
37. IAEA, Live Chart of Nuclides, Interractive Chart of Nuclides (International Atomic Energy, 2009) available at `https://www-nds.iaea.org/`.
38. M.B. Chadwick, M. Herman, P. Obložinský, M.E. Dunn, Y. Danon, A.C. Kahler, D.L. Smith, B. Pritychenko, G. Arbanas, R. Arcilla, R. Brewer, D.A. Brown, R. Capote, A.D. Carlson, Y.S. Cho, H. Derrien, K. Guber, G.M. Hale, S. Hoblit, S. Holloway, T.D. Johnson, T. Kawano, B.C. Kiedrowski, H. Kim, S. Kunieda, N.M. Larson, L. Leal,

J.P. Lestone, R.C. Little, E.A. McCutchan, R.E. MacFarlane, M. MacInnes, C.M. Mattoon, R.D. McKnight, S.F. Mughabghab, G.P.A. Nobre, G. Palmiotti, A. Palumbo, M.T. Pigni, V.G. Pronyaev, R.O. Sayer, A.A. Sonzogni, N.C. Summers, P. Talou, I.J. Thompson, A. Trkov, R.L. Vogt, S.C. van der Marck, A. Wallner, M.C. White, D. Wiarda, P.G. Young, Nucl. Data Sheets **112**, 2887 (2011).

39. D.W. Millsap, S. Landsberger, Appl. Radiat. Isot. **97**, 21 (2015).
40. E. Robu, C. Giovani, Rom. Rep. Phys. **61**, 295 (2009).
41. R. Nowotny, *XMuDat: Photon attenuation data on PC*, IAEA Report IAEA-NDS, 195 (1998) available at `https://www-nds.iaea.org/publications/iaea-nds/iaea-nds-0195.htm`.
42. D.L. Smith, Nucl. Instrum. Methods Phys. Res. A **257**, 365 (1987).
43. S.S. Yerraguntla, H. Naik, M.P. Karantha, S. Ganesan, S.V. Suryanarayana, S. Badwar, J. Radioanal. Nucl. Chem. **314**, 457 (2017).
44. R. Ghosh, S. Badwar, B. Lawriniang, Y.S. Sheela, H. Naik, Y. Naik, S.V. Suryanarayana, B. Jyrwa, S. Ganesan, J. Radioanal. Nucl. Chem. **314**, 1983 (2017).
45. A.J. Koning, D. Rochman, J. Kopecky, J.Ch. Sublet, M. Fleming, E. Bauge, S. Hilaire, P. Romain, B. Morillon, H. Duarte, S.C. van der Marck, S. Pomp, H. Sjostrand, R. Forrest, H. Henriksson, O. Cabellos, S. Goriely, J. Leppanen, H. Leeb, A. Plompen, R. Mills, `https://tendl.web.psi.ch/tendl_2015`.
46. Z.G. Ge, Z.X. Zhao, H.H. Xia, Y.X. Zhuang, T.J. Liu, J.S. Zhang, H.C. Wu, J. Kor. Phys. Soc. **59**, 1052 (2011).
47. K. Shibata, O. Iwamoto, T. Nakagawa, N. Iwamoto, A. Ichihara, S. Kunieda, S. Chiba, K. Furutaka, N. Otuka, T. Ohasawa, T. Murata, H. Matsunobu, A. Zukeran, S. Kamada, J. Katakura, J. Nucl. Sci. Technol. **48**, 1 (2011).
48. A.J. Koning, E. Bauge, C.J. Dean, E. Dupont, U. Fischer, R.A. Forrest, R. Jacqmin, H. Leeb, M.A. Kellett, R.W. Mills, C. Nordborg, M. Pescarini, Y. Rugama, P. Rullhusen, J. Kor. Phys. Soc. **59**, 1057 (2011).